Molecular Mechanism of PP2A/B55α Inhibition by IER5

Ruili Cao[1#], Daniel TD Jones[1#], Li Pan[2], Shumei Wang[2], Shaun Rawson[1], Jon C Aster[2*], and Stephen C Blacklow[1,3*]

[1]Department of Biological Chemistry and Molecular Pharmacology, Blavatnik Institute, Harvard Medical School, Boston, MA USA

[2]Department of Pathology, Brigham and Women's Hospital, Boston, MA USA

[3]Department of Cancer Biology, Dana Farber Cancer Institute, Boston, MA USA

[#]Equal contributors

*Correspondence: stephen_blacklow@hms.harvard.edu; jaster@rics.bwh.harvard.edu

ABSTRACT

PP2A serine/threonine protein phosphatases are heterotrimeric complexes that have a wide range of essential physiologic functions. The B55α form of PP2A has critical roles in cell cycle regulation, mitotic exit, and the DNA damage response[1-6]. Its activity is modulated by additional regulatory proteins, such as ARPP19[7], FAM122A[8], and IER5[9]. However, the precise mechanisms underlying the modulation of PP2A activity by these proteins remain elusive. Here, we show that IER5 inhibits pTau dephosphorylation by PP2A/B55α in biochemical assays and report a cryoelectron microscopy structure of the PP2A/B55α-IER5 complex, which reveals that IER5 occludes a surface on B55α used for substrate recruitment[10-12]. Mutation of interface residues on IER5 interferes with recovery of B55α in co-immunoprecipitation assays and suppresses events in squamous carcinoma cells, such as *KRT1* expression, that depend on inhibition of PP2A/B55α by IER5[9]. These studies define the molecular basis for PP2A inhibition by IER5 and suggest a roadmap for selective pharmacologic modulation of PP2A/B55α complexes.

Main

PP2A serine/theonine protein phosphatases are assembled from a scaffolding subunit (A, A'), a catalytic subunit (C, C') and a regulatory subunit derived from one of four different protein subfamiliies (B/B55, B'/B56, B''/PR48-PR70, and B'''/striatin)[13]. In addition to its role in regulating the cell cycle and the DNA damage response, the PP2A A-C subcomplex is also incorporated into the INTAC submodule of the integrator complex regulating gene transcription [14,15].

IER5 is a member of the AP1-regulated immediate early response (IER) gene family[16], encoding a protein of 327 amino acids. Expression of IER5 is induced in response to ionizing radiation, and IER5 is implicated in the cellular response to DNA damaging agents and heat shock[17-19]. In squamous cell carcinoma (SCC) cells, *IER5* is a direct transcriptional target of activated Notch. Expression of IER5 in response to Notch activation in these SCC cells is required for induction of a cell differentiation program that arrests cell growth and stimulates expression of *KRT1* and other keratinocyte-associated genes[9] .

IER5 executes its cellular function, at least in part, by binding to and modulating the activity of heterotrimeric B55α holoenzyme complexes of PP2A[9,20-22]. Though one proposed model for IER5 function proposes that it acts to direct selection of substrates such as S6K and HSF1[22], IER5 functions as a PP2A/B55α antagonist in SCC cells, where its suppression of PP2A/B55α activity is necessary for Notch-dependent induction of genes associated with keratinocyte differentiation [9]. Here, we report the structure of a PP2A/B55α-IER5 complex, uncovering the molecular basis for its function as an inhibitor of PP2A/B55α, and identifying a strategy for selective modulation of PP2A/B55α activity.

Results

IER5 inhibits PP2A dephosphorylation of pTau. Previous work demonstrated that the 50-residue N-terminal IER domain of IER5, predicted to be a helical hairpin by alphafold2 (**Extended Data Fig. 1**), is necessary and sufficient for binding to B55α/PP2A, whereas the C-terminal region, predicted to be unstructured (**Extended Data Fig. 1**), does not interact[9]. We purified the PP2A/B55α holoenzyme both in isolation and in complex with the IER5 N-terminal domain (**Extended Data Fig. 2**), and compared the dephosphorylation activity of the two complexes

using phosphorylated Tau (pTau) as substrate[12] (**Fig. 1a,b**). The rate of pTau dephosphorylation was approximately 5-fold slower when PP2A/B55α was complexed with IER5 (**Fig. 1c**), showing that IER5 acts as an inhibitor of protein substrate dephosphorylation.

Structure of a PP2A/B55α-IER5 complex. To elucidate the molecular basis for IER5-dependent inhibition of PP2A/B55α substrate dephosphorylation, we determined a structure of the complex using single particle electron cryomicroscopy (cryo-EM; **Fig. 2 and Extended Data Figs. 3-4**). During data processing, we observed that PP2A-IER5 complexes existed in both monomeric and dimeric assemblies (**Extended Data Fig. 3**). We utilized both assemblies during refinement to minimize anisotropy, and produced a final map of the monomeric assembly with a resolution of 3.09 Å. Using a local mask, we also refined a focused map around B55α, IER5 and part of the scaffolding subunit to 3.13 Å. An alphafold model of the PP2A/B55α-IER5 complex created with alphafold multimer[23] was then docked into the combined and focused cryo-EM maps before refinement to produce the final models (see methods).

IER5 adopts a helical hairpin conformation in the complex, and exclusively contacts the B55α subunit. Complexation of PP2A/B55α with IER5 increases the curvature of the scaffolding subunit, resulting in a 22 Å displacement of its C-terminus upon binding and closer approximation of the B55α and catalytic subunits (**Extended Data Fig. 5**). It is also possible to model the C-terminal end of the catalytic subunit in the complex, which extends across a gap between the regulatory and catalytic subunits to engage the third blade of the B55α β-propeller. Prior work suggests that LCMT1 methylation of the C-terminal end of the PP2A catalytic subunit facilitates holoenzyme assembly[24,25], but our local resolution at this site is not sufficient to unambiguously identify this modification.

Interface between IER5 and PP2A. The IER5-B55α interface buries a total surface area of 2367 $Å^2$ (**Fig. 2c**). This interface includes a predominantly hydrophobic contact surface toward the N- and C-termini of the helical hairpin, and a site with electrostatic complementarity between a basic region of IER5 centered on the loop connecting the helices and a series of acidic residues on B55α (**Fig. 2d**). Among the residues at the hydrophobic interface at the top of IER5 are I10, L35, and V39, which pack into pockets created by F280, F281, I284, F343 and Y337 of B55α (**Fig. 3a**). Adjacent to the hydrophobic interface there is also a hydrogen bond between the phenolic hydroxyl of Y337 and the S14 side chain hydroxyl group (**Fig. 3a**)**,** which also lies within hydrogen bonding distance of the backbone carbonyl of I10. At the interface around the IER5 loop between helices, R25 of IER5 protrudes into a negatively charged groove created by E91 and E93 of B55α. (**Fig. 3b**), engaging in a salt bridge with the carboxylate group of E93. K32 of IER5 engages in a charged hydrogen bond with D340 of B55α and makes aliphatic contact with F343. There is also a charged hydrogen bond between H31 of IER5 and S287 of B55α. K17 and K29 of IER5 also contribute to the positively charged electrostatic surface on IER5 that complements the acidic B55α surface (**Fig. 2d**).

To test the importance of the hydrophobic and electrostatic IER5 surfaces in complex formation with B55α, we introduced single point mutations into full-length IER5 at interface residues or control mutations at sites distant from the contact interface (L15 and N20 of IER5; **Fig. 3c**) and tested their effects on B55α binding in a co-immunoprecipitation assay in IER5 knockout cells (**Fig. 3d**). Wild-type IER5, the IER5 L15R mutant, and the N20A mutant all strongly co-immunoprecipitated B55α. In contrast, the interface mutations either completely prevented (S14A, K17E, L30E), or greatly reduced (I10A, R25E, K29E, H31A, K32E, L35A, V39A) co-

immunoprecipitation of B55α (**Fig. 3c**), confirming that the interface seen in the cryo-EM structure is required for binding of IER5 to B55α in cells.

Interface-disrupting mutations block IER5-dependent induction of KRT1 transcription. In the SCC cell line SC2, IER5 is needed for Notch-dependent induction of *KRT1* expression (**Fig. 4a**), a requirement that is relieved when B55α is knocked out and restored when wild-type IER5 is reintroduced into IER5 knockout, B55α wild-type SC2 cells[9] (**Fig. 4b**). Reintroduction of the L15R or N20A control mutants of IER5 also rescues expression of KRT1 in response to Notch activation (**Fig. 4b**). In contrast, the I10A, S14A, K17E, and L30E interface disrupting mutations all greatly reduce *KRT1* expression, as determined by RT-qPCR (**Fig. 4b**). These data show that interfering with the binding of IER5 to B55α leads to a loss of IER5 function in SC2 cells.

Discussion

The work reported here shows that the N-terminal helical hairpin of IER5 acts as an inhibitor of PP2A/B55α phosphatase activity by occluding the substrate-binding platform of the B55α regulatory subunit. In complex with PP2A/B55α, IER5 masks an extensive region on the surface of B55α that faces the catalytic subunit but does not directly contact the catalytic subunit itself.

Substrate recruitment to B55α relies primarily on short linear motifs (SLiMs), which may adopt an alpha helical conformation when bound[10] . Mapping of residues on B55α that reportedly participate in substrate recruitment shows substantial overlap with the IER5 binding site[10-12] (**Extended Data Fig. 6**). The mode of IER5 binding differs, however, from that predicted for the inhibitors FAM122A and ARPP19, which have both been proposed to engage the B55α subunit

with a short helical motif and bridge to the catalytic subunit using a discontinuous unstructured segment[26].

In our studies with purified complexes, we observed incomplete inhibition of pTau dephosphorylation (**Fig. 1**). This finding may stem from limitations in our assay for inhibition of PP2A/B55α. Because we were unable to purify IER5 for addition in trans to purified PP2A/B55α, it was necessary to directly compare the activity of free PP2A/B55α with the IER5-complexed form of PP2A/B55α, purified separately. It was thus possible that some of the IER5 dissociated from the complex during storage or during the course of the reaction. We also cannot exclude the possibility that phosphorylated serines or negatively charged glutamates present in a conserved region near the C-terminus of IER5 (**Extended Data Fig. 7**), which is predicted to be natively unstructured, are used to occupy the active site of the C-subunit and further potentiate inhibition. Alternatively, as others have proposed, it is also possible that the exposed face of IER5 does not preclude some access of pTau to the PP2A active site, and is even able, under certain circumstances, to bind to a different cohort of proteins than the B55α substrate-recruitment platform, and thereby alter the substrate selectivity of the phosphatase when complexed with IER5[22].

The immediate early response genes also include a family member called IER3 (also known as IEX-1), which is closely related to IER5. IER3 inhibits the activity of the PP2A/B56 isoform by promoting the dissociation of B56 from the active enzyme[27,28]. Of interest, *IER3* also appears to be a direct target of Notch signaling in SCC cells[9]. The induction of different immediate early response proteins by Notch and cell stresses such as radiation-induced DNA damage may

serve to induce cell cycle arrest and differentiation of squamous cells through the coordinated inhibition of multiple PP2A holoenzyme species.

Lastly, there is interest in development of PP2A modulators for diseases ranging from neurodegeneration to cancer[29,30]. The IER5 contact site could serve as a target surface for developing protein-protein interaction (PPI) inhibitors that selectively block substrate recruitment to PP2A/B55α complexes, or conversely, for molecular glue modulators that can direct dephosphorylation of specific proteins, analogous to protein-degrading IMiDs[31].

Acknowledgements

We thank the Cryo-EM Center for Structural Biology at Harvard Medical School for help and advice with data collection, and members of the Blacklow lab and Alan Brown for helpful discussions.

Funding

This work was supported by NIH award 1R35 CA220340 (to SCB), the Ludwig Center at Harvard (JCA), and the Blavatnik Institute of Harvard Medical School.

Author Contributions

JCA and SCB conceived the project and acquired funding. RC purified PP2A/B55α-IER5 complexes, acquired biochemical data, prepared samples for cryo-EM data collection, and collected cryo-EM images. DTDJ processed and analyzed cryo-EM data with input from SR and

RC, and DTDJ built the structural models. LP performed co-immunoprecipitation studies and *KRT1* expression analyses. All authors participated in data analysis and interpretation. SCB, RC, DTDJ and JCA wrote and edited the manuscript with input from all authors. All authors agreed on the final manuscript.

Competing Interests

SCB is on the board of directors of the non-profit Institute for Protein Innovation and the Revson Foundation, is on the scientific advisory board for and receives funding from Erasca, Inc. for an unrelated project, is an advisor to MPM Capital, and is a consultant for IFM, Scorpion Therapeutics, Odyssey Therapeutics, Droia Ventures, and Ayala Pharmaceuticals for unrelated projects. JCA is a consultant for Ayala Pharmaceuticals, Cellestia, Inc., SpringWorks Therapeutics, and Remix Therapeutics. The other authors declare that they have no competing interests.

Methods

Plasmid construction

cDNAs encoding PPP2R1A, PPP2CA and PPP2R2A (B55α) assembled in a pAC-derived baculovirus expression vector (pAC8RedNK) were gifts from the Fischer lab (Dana Farber Cancer Institute). PPP2R1A was engineered to include an N-terminal His_6 tag followed by a Tobacco etch virus (TEV) cleavage site, the cDNA for PPP2R2A (B55α) had no affinity tag, and PPP2CA had an N-terminal Flag tag followed by a TEV cleavage site. The IER5 (1-50) fragment

was subcloned into pAC8RedNK with an N-terminal Strep tag II followed by a TEV cleavage site. The full-length Tau protein was cloned into the bacterial expression vector ptd68, incorporating an N-terminal His_6-SUMO tag. Insert sequences were confirmed by Sanger sequencing.

Protein Expression

The PP2A-B55α heterotrimer and the PP2A-IER5 complex were expressed in Sf9 cells. 1.5 µg of the pAC8RedNK vector and 0.5 µg of linearized baculoviral DNA were concurrently transfected into $1x10^6$ Sf9 cells using 6 µl of FuGene HD (Promega) in ESF 921 Insect Cell Culture medium (Expression Systems). After 5 to 7 days of incubation, the supernatant was collected to harvest the baculovirus. The virus was subsequently amplified for 2 to 3 cycles using Sf9 cells at a concentration of $2x10^6$. The collected viruses were then used to infect Hi5 cells for protein expression. For expression of the PP2A heterotrimer, a viral stoichiometric ratio of 1:1:1 was used for Hi5 cell infection. For the PP2A-IER5 complex, a ratio of 1:1:1:1.5 (IER5) was used. Cells were shaken at 27 °C for 72 hours before harvesting by centrifugation. Cell pellets were collected and stored at −80 °C until purification.

Recombinant Tau protein was expressed in E. coli BL21 (DE3) cells. Protein expression was induced at a culture optical density (OD) of 0.8 by addition of 0.2 mM isopropyl-1-thio-D-galactopyranoside (IPTG) and the culture was maintained at 16°C overnight. Cell pellets were collected and stored at −80 °C until purification.

Protein purification

For the PP2A heterotrimer, cells were resuspended in lysis buffer containing 20mM Tris-HCl, pH 7.6, 200mM NaCl, 2mM Tris-(2-carboxyethyl) phosphine (TCEP), 0.1% (v/v) Triton X-100, protease inhibitor cocktail (Sigma) and Benzonase (EMD Millipore). Cells were lysed by sonication and centrifuged at 50,000 *g* for 1 h. The soluble fraction was passed over an anti-FLAG M2 affinity resin. The resin was washed with 10 column volumes (CVs) of wash buffer (20 mM Tris-HCl, pH 7.6, 200 mM NaCl, 2 mM TCEP), and the protein was then eluted using wash buffer supplemented with 0.2 mg/ml of FLAG peptide. The elution fractions were collected, concentrated, and further purified using size-exclusion chromatography (SEC) on a Superdex S200 10/300 column, which was pre-equilibrated with buffer (20 mM Tris-HCl, pH 7.6, 200 mM NaCl, 2 mM TCEP). Protein purity was assessed by SDS-PAGE using a Coomassie blue stain. Peak fractions were pooled for biochemical studies.

For the PP2A-IER5 complex, lysis and ultracentrifugation was performed as above. The affinity purification step was performed using Strep-Tactin XT Superflow resin (IBA), followed by elution with wash buffer supplemented with 50 mM biotin. After elution from the column the fractions were concentrated and further purified using size exclusion chromatography on a Superdex S200 10/300 column as above. Protein purity was assessed by SDS-PAGE using a Coomassie blue stain. Peak fractions were pooled for biochemical studies and for Cryo-EM data collection.

For preparation of Tau protein, bacterial cells were resuspended in lysis buffer containing 20 mM Tris-HCl, pH 8, 200 mM NaCl, 2 mM Tris-(2-carboxyethyl) phosphine (TCEP), protease inhibitor cocktail (Sigma), 20 mM Imidazole. Cells were lysed by sonication and centrifuged to remove debris. After centrifugation, the supernatant containing the recombinant His-SUMO-Tau was applied to Ni(NTA) affinity resin, and the resin was washed using the lysis buffer. The His-SUMO

tag was removed overnight by on-column cleavage with ULP1 protease. Protease-liberated Tau was recovered from the column flow-through and was further purified by size exclusion chromatography using a Superdex 75 10/300 GL (GE Healthcare) column, in buffer consisting of 20 mM Tris-HCl pH 8, 200 mM NaCl, and 2mM TCEP. Peak fractions were pooled for phosphorylation using GSK3β. The concentration of purified Tau was determined by UV absorbance at 280 nm.

Phosphorylation of Tau protein and purification of pTau

Purified Tau was incubated with GSK3β (SinoBiological) in a 100:1 ratio, using a buffer of 25 mM HEPES pH 7.5, containing 100 mM NaCl, 10 mM $MgCl_2$, 10 mM ATP, and 2 mM TCEP. The reaction was allowed to proceed for 19 hours at 37 ^{o}C. Verification that the reaction had gone to completion was performed by SDS-PAGE with Coomassie blue staining. The pTau was further purified by size exclusion chromatography using a Superdex 75 10/300 GL (GE Healthcare) column in buffer consisting of 20 mM Tris-HCl pH 8, 200 mM NaCl, and 2mM TCEP. The concentration of purified pTau was determined by UV absorbance at 280 nm. Fractions were collected and frozen in -80 prior to use.

Cryo-EM grid preparation and data collection

Samples were frozen on Cryo-EM grids using a Vitrobot Mark IV (Thermo Fisher Scientific) instrument for vitrification. 3.5 µl of freshly purified PP2A-IER5 complex, at a concentration of 2 mg/ml, was deposited onto glow-discharged C-flat holey carbon grids (R1.2/1.3, 400 mesh copper, Electron Microscopy Sciences). These grids were blotted for 6 seconds with a blot force of 15 at 100% humidity and 22 degrees C before being rapidly submerged into liquid ethane that had been cooled by liquid nitrogen for plunge freezing.

Images were acquired on a Titan Krios microscope equipped with a BioQuantum K3 Imaging Filter (slit width 25 eV) and a K3 direct electron detector (Gatan), operating at an acceleration voltage of 300 kV. Images were recorded at a defocus range of −0.8 to −2.0 μm with a nominal magnification of 105 kx, resulting in a pixel size of 0.825 Å. Each image was dose fractionated into 51 movie frames with a total exposure time of 2.8 s, resulting in a total dose of ~53.7 electrons per $Å^2$. SerialEM was used for data collection.

Structure Determination

Data were processed using CryoSPARC[32], as summarized in **Extended Data Fig. 3**. A total of 5383 micrographs were subjected to patch motion correction and patch CTF estimation. 3.95 million particles were identified and extracted using a box size of 360 pixels using the CryoSPARC blob picker. 2D classification was used to remove poorly classifying particles, reducing the total number of particles to 1.17 million. From the projected 2D class averages, a mixture of monomeric and dimeric PP2A-IER5 assemblies was evident. 100,000 particles were split and used to generate three preliminary maps to represent the different species present in the data. The three maps were subjected to heterogeneous refinement using all identified particles, resulting in three classes designated as monomeric (~47 %), dimeric (~25 %) and junk (~27 %) (e.g., scaffolding subunit only) classes. The monomeric and dimeric classes were then processed independently. Non-uniform refinement, local motion correction, and then another round of non-uniform refinement was applied to the monomer class, yielding a map with a nominal resolution of 3.67 Å, with reasonable anisotropy (cryoEF = 0.71[33]). The monomer class displayed no clear IER5 density at this stage of processing. Non-uniform refinement, local motion correction, and then another round of non-uniform refinement was applied to the dimeric

class, resulting in a resolution of 3.67 Å for the dimer class map. Alignment of the dimeric map along an apparent C2 symmetry axis followed by non-uniform refinement under a C2 symmetry constraint improved the map to 3.44 Å resolution. A further round of local motion correction and two rounds of sequential non-uniform refinement produced a map of 3.17 Å resolution. To resolve symmetry breaking features, symmetry expansion was performed along the C2 symmetry axis. Masked local refinement with a soft mask around a single copy from an asymmetric unit, produced a map at 3.04 Å resolution. Despite this reasonable global resolution, the map displayed strong directional anisotropy (cryoEF = 0.46[33]).

Masked non-uniform refinement using a single copy of an asymmetric unit of the symmetry expanded dimer map, using the monomeric particles as input, resulted in a 3.82 Å map with improved signal for IER5. We then combined all the aligned monomer and symmetry expanded dimer particles and performed a masked local refinement that resulted in a combined map of 3.09 Å resolution with improved directional isotropy (cryoEF = 0.68). We finally performed a local refinement on the combined map with a mask that enveloped all IER5, B55α, and the scaffolding subunit HEAT repeats 1-9 (residues 1-355), resulting in a focused map of 3.13 Å resolution (cryoEF = 0.71).

Model refinement and atomic model building

Initial models were generated using alphafold. The models were fitted to the map using MOLREP[34], and the initial model-to-map fit was improved using ISOLDE[35]. The model was refined using REFMAC Servalcat[36], preliminarily using restraints generated from PDB 3DW8 using ProSMART[37], followed by sequential rounds of jelly body refinement. The model was refined in Phenix using Phenix Real-Space Refine[38] before manual inspection and refinement in

Coot[39]. The final models were evaluated using MolProbity[40]. Statistics of the map reconstruction and model refinement are presented in Extended Data Table 1. Structural biology applications used in this project (except CryoSPARC) were compiled and configured by SBGrid[41]. Molecular graphics and analyses were performed with UCSF ChimeraX[42] (developed by the Resource for Biocomputing, Visualization, and Informatics at the University of California, San Francisco, with support from National Institutes of Health R01-GM129325 and the Office of Cyber Infrastructure and Computational Biology, National Institute of Allergy and Infectious Diseases), or PyMOL (Schrödinger).

Cell culture

Cells were grown under 5% CO2 at 37°C in media supplemented with streptomycin/penicillin. IER5 knock-out cell line I5[9] was derived from SC2 cells, which are engineered to contain a cDNA encoding a mutated truncated form of NOTCH1, ΔEGF-L1596H, that is regulatable with a γ-secretase inhibitor (GSI) [9] . I5 and its derivatives overexpressing wide-type and mutant IER5 were cultured in Keratinocyte medium as described[43] in the presence of GSI (1μM compound E) to maintain Notch in the off-state. Timed activation of Notch was triggered by GSI washout as described [9].

Expression Constructs, Viral Production and Infection of Cells.

The expression vector MIEG3-IER5-FH was constructed by inserting human IER5 tagged with HA and 3XFLAG into MIEG3 vector (Pan et al), which is a murine stem cell virus (MSCV)-based bicistronic retroviral construct expressing EGFP. MIEG3 expression vectors containing IER5 mutations were generated by QuickChange II Site-Directed Mutagenesis Kit (Agilent).

Retrovirus was prepared by transfecting Phoenix-gp cells with the MIEG3 vector and expression vectors for Gag/Pol and GALV. Viral supernatant was collected 48h posttransfection, centrifuged, and filtered through a 0.45 μm filter (Corning). For infection of target cells, 1 ml of virus was mixed with cells and protamine sulfate in a 6-well plate, and the plate was then centrifuged at 2,250 rpm for 90 min at room temperature. GFP-expressing cells were then isolated by cell-sorting 24 hr after transduction as described [9].

Quantitative RT-PCR

After 72 hours of GSI washout, cells were resuspended in Trizol (Life Technologies), and total RNA was prepared with RNeasy Mini kit (Qiagen). cDNA was synthesized with the High Capacity cDNA Reverse Transcripition Kit (Applied Biosystems). PCR was performed using the PowerUP SYBR Green Master Mix (Applied Biosystems) with the QuantStudio 3 Real-Time PCR System (Applied Biosystems). Primers used for *KRT1* and *GAPDH* are: forward 5'-GGACAGCTCCTTAGCATCTTATC-3', reverse 5'-GGAGTTTAAGACCTCTCCACAAA-3' and forward 5'-GAAGGTGAAGGTCGGAGTCAAC-3', reverse 5'-TGGAAGATGGTGATGGGATTTC-3', respectively.

Immunoprecipitation and Western Blotting

For immunoprecipitation assays, cells in 10-cm dishes were washed in cold PBS and lysed in 1 ml of Pierce IP Lysis Buffer (Thermo Scientific) supplemented with protease inhibitors (Sigma). Cell lysates with equal amounts of protein were incubated with 25μl of washed Pierce Anti-HA Magnetic Beads (Thermo Scientific) overnight at 4°C with mixing. The beads were then washed three times with TBS-T and once with ultrapure water. The HA-tagged IER5 and its associated proteins were eluted with Pierce HA peptide (Themo Scientific). The eluates and input proteins

were loaded on 3-8% SDS-polyacrylamide gels and resolved by electrophoresis. Proteins were incubated at 4 C overnight following transfer to nitrocellulose membranes with the following primary antibodies: anti-PP2A B55 (100C1) and anti-HA (C29F4) (both from Cell Signaling Technology); anti-IER5 (HPA029894) and anti-Flag (F3165) (both from Sigma). Secondary antibody was either goat anti-rabbit (7074) or horse anti-mouse (7076) IgG conjugated with horseradish peroxidase (Cell Signaling Technology). Staining was developed with SuperSignal West Dura Extended Duration Substrate (Thermo Scientific) for 2min at room temperature and documented by exposure to x-ray film.

1 Grallert, A. *et al.* A PP1-PP2A phosphatase relay controls mitotic progression. *Nature* **517**, 94-98 (2015).

2 Krasinska, L. *et al.* Protein phosphatase 2A controls the order and dynamics of cell-cycle transitions. *Mol Cell* **44**, 437-450 (2011).

3 Swartz, S. Z. *et al.* Selective dephosphorylation by PP2A-B55 directs the meiosis I-meiosis II transition in oocytes. *Elife* **10** (2021).

4 Kalev, P. *et al.* Loss of PPP2R2A inhibits homologous recombination DNA repair and predicts tumor sensitivity to PARP inhibition. *Cancer Res* **72**, 6414-6424 (2012).

5 Wurzenberger, C. & Gerlich, D. W. Phosphatases: providing safe passage through mitotic exit. *Nature Reviews Molecular Cell Biology* **12**, 469-482 (2011).

6 Schmitz, M. H. A. *et al.* Live-cell imaging RNAi screen identifies PP2A-B55alpha and importin-beta1 as key mitotic exit regulators in human cells. *Nat Cell Biol* **12**, 886-893 (2010).

7 Gharbi-Ayachi, A. *et al.* The substrate of Greatwall kinase, Arpp19, controls mitosis by inhibiting protein phosphatase 2A. *Science* **330**, 1673-1677 (2010).

8 Li, F. *et al.* CHK1 Inhibitor Blocks Phosphorylation of FAM122A and Promotes Replication Stress. *Mol Cell* **80**, 410-422 e416 (2020).

9 Pan, L. *et al.* IER5, a DNA damage response gene, is required for Notch-mediated induction of squamous cell differentiation. *Elife* **9** (2020).

10 Fowle, H. *et al.* PP2A/B55alpha substrate recruitment as defined by the retinoblastoma-related protein p107. *Elife* **10** (2021).

11 Cundell, M. J. *et al.* A PP2A-B55 recognition signal controls substrate dephosphorylation kinetics during mitotic exit. *J Cell Biol* **214**, 539-554 (2016).

12 Xu, Y., Chen, Y., Zhang, P., Jeffrey, P. D. & Shi, Y. Structure of a Protein Phosphatase 2A Holoenzyme: Insights into B55-Mediated Tau Dephosphorylation. *Mol Cell* **31**, 873-885 (2008).

13 Amin, P. *et al.* PP2A-B55: substrates and regulators in the control of cellular functions. *Oncogene* **41**, 1-14 (2022).

14 Huang, K. L. *et al.* Integrator Recruits Protein Phosphatase 2A to Prevent Pause Release and Facilitate Transcription Termination. *Mol Cell* **80**, 345-358 e349 (2020).
15 Zheng, H. *et al.* Identification of Integrator-PP2A complex (INTAC), an RNA polymerase II phosphatase. *Science* **370** (2020).
16 Williams, M. *et al.* Ier5, a novel member of the slow-kinetics immediate-early genes. *Genomics* **55**, 327-334 (1999).
17 Ding, K. K. *et al.* Induced expression of the IER5 gene by gamma-ray irradiation and its involvement in cell cycle checkpoint control and survival. *Radiat Environ Biophys* **48**, 205-213 (2009).
18 Ishikawa, Y. & Sakurai, H. Heat-induced expression of the immediate-early gene IER5 and its involvement in the proliferation of heat-shocked cells. *FEBS J* **282**, 332-340 (2015).
19 Kis, E. *et al.* Microarray analysis of radiation response genes in primary human fibroblasts. *Int J Radiat Oncol Biol Phys* **66**, 1506-1514 (2006).
20 Asano, Y. *et al.* IER5 generates a novel hypo-phosphorylated active form of HSF1 and contributes to tumorigenesis. *Sci Rep* **6**, 19174 (2016).
21 Ishikawa, Y., Kawabata, S. & Sakurai, H. HSF1 transcriptional activity is modulated by IER5 and PP2A/B55. *FEBS Lett* **589**, 1150-1155 (2015).
22 Kawabata, S., Ishita, Y., Ishikawa, Y. & Sakurai, H. Immediate-early response 5 (IER5) interacts with protein phosphatase 2A and regulates the phosphorylation of ribosomal protein S6 kinase and heat shock factor 1. *FEBS Lett* **589**, 3679-3685 (2015).
23 Evans, R. *et al.* Protein complex prediction with AlphaFold-Multimer. *bioRxiv* (2022).
24 Stanevich, V. *et al.* The structural basis for tight control of PP2A methylation and function by LCMT-1. *Mol Cell* **41**, 331-342 (2011).
25 Tolstykh, T., Lee, J., Vafai, S. & Stock, J. B. Carboxyl methylation regulates phosphoprotein phosphatase 2A by controlling the association of regulatory B subunits. *EMBO J* **19**, 5682-5691 (2000).
26 Wasserman, J. S. *et al.* FAM122A ensures cell cycle interphase progression and checkpoint control as a SLiM-dependent substrate-competitive inhibitor to the B55α/PP2A phosphatase. *bioRxiv* (2023).
27 Letourneux, C., Rocher, G. & Porteu, F. B56-containing PP2A dephosphorylate ERK and their activity is controlled by the early gene IEX-1 and ERK. *EMBO J* **25**, 727-738 (2006).
28 Rocher, G., Letourneux, C., Lenormand, P. & Porteu, F. Inhibition of B56-containing protein phosphatase 2As by the early response gene IEX-1 leads to control of Akt activity. *J Biol Chem* **282**, 5468-5477 (2007).
29 Clark, A. R. & Ohlmeyer, M. Protein phosphatase 2A as a therapeutic target in inflammation and neurodegeneration. *Pharmacol Ther.* **201**, 181-201 (2019).
30 Ronk, H., Rosenblum, J. S., Kung, T. & Zhuang, Z. Targeting PP2A for cancer therapeutic modulation. *Cancer Biol Med* **19**, 1428-1439 (2022).
31 Fischer, E. S. *et al.* Structure of the DDB1-CRBN E3 ubiquitin ligase in complex with thalidomide. *Nature* **512**, 49-53 (2014).
32 Punjani, A., Rubinstein, J. L., Fleet, D. J. & Brubaker, M. A. cryoSPARC: algorithms for rapid unsupervised cryo-EM structure determination. *Nat Methods* **14**, 290-296 (2017).
33 Naydenova, K. & Russo, C. J. Measuring the effects of particle orientation to improve the efficiency of electron cryomicroscopy. *Nat Commun* **8**, 629 (2017).
34 Vagin, A. & Teplyakov, A. MOLREP: an Automated Program for Molecular Replacement. *Journal of Applied Crystallography* **30**, 1022-1025 (1997).
35 Croll, T. I. ISOLDE: a physically realistic environment for model building into low-resolution electron-density maps. *Acta Crystallogr D Struct Biol* **74**, 519-530 (2018).

36 Yamashita, K., Palmer, C. M., Burnley, T. & Murshudov, G. N. Cryo-EM single-particle structure refinement and map calculation using Servalcat. *Acta Crystallogr D Struct Biol* **77**, 1282-1291 (2021).
37 Nicholls, R. A., Fischer, M., McNicholas, S. & Murshudov, G. N. Conformation-independent structural comparison of macromolecules with ProSMART. *Acta Crystallogr D Biol Crystallogr* **70**, 2487-2499 (2014).
38 Afonine, P. V. *et al.* Real-space refinement in PHENIX for cryo-EM and crystallography. *Acta Crystallogr D Struct Biol* **74**, 531-544 (2018).
39 Casanal, A., Lohkamp, B. & Emsley, P. Current developments in Coot for macromolecular model building of Electron Cryo-microscopy and Crystallographic Data. *Protein Sci* **29**, 1069-1078 (2020).
40 Williams, C. J. *et al.* MolProbity: More and better reference data for improved all-atom structure validation. *Protein Sci* **27**, 293-315 (2018).
41 Morin, A. *et al.* Collaboration gets the most out of software. *Elife* **2**, e01456 (2013).
42 Pettersen, E. F. *et al.* UCSF ChimeraX: Structure visualization for researchers, educators, and developers. *Protein Sci* **30**, 70-82 (2021).
43 Purdie, K. J., Pourreyron, C. & South, A. P. Isolation and culture of squamous cell carcinoma lines. *Methods Mol Biol* **731**, 151-159 (2011).
44 Jumper, J. *et al.* Highly accurate protein structure prediction with AlphaFold. *Nature* **596**, 583-589 (2021).
45 Ashkenazy, H. *et al.* ConSurf 2016: an improved methodology to estimate and visualize evolutionary conservation in macromolecules. *Nucleic Acids Res* **44**, W344-350 (2016).

Figure Legends

Fig. 1 – Tau dephosphorylation assay. a, SYPRO(R) Ruby stained SDS-PAGE gel of 100 nM PP2A complex purified alone (left) and with IER5 (right). **b**, Anti-pTau (S396) Western blot comparing the pTau phosphatase activity of PP2A purified in the absence (left) and presence (right) of IER5. **c**, Densitometry analysis of bands observed in **(b)**. Data are presented as mean ± s.d. of three biological replicates. Data are normalized to time point t=0. The Welch t-test statistic was used to compare the means between each PP2A and PP2A-IER5 time point *(*P*<0.05, ***P*<0.01, ****P*<0.001, and *****P*<0.0001).

Fig. 2 Cryo-EM structure of a PP2A-IER5 complex and interface analysis. a, Cryo-EM map of the PP2A-IER5 complex. The scaffolding A subunit is green, the regulatory B55α subunit is magenta, the catalytic C subunit is wheat and IER5 is cyan. **b,** Cartoon rendering of the modelled structure, colored as in (**a**), with manganese atoms of the catalytic subunit rendered as grey spheres. **c,** Open book view depicting the interface between B55α and IER5. IER5 is cyan, and B55α is blue. Residues at the contact interface in the complex (center), on B55α (left), and on IER5 (right) are colored in a darker shade. **d,** Electrostatic surface representation of the complex (center), of B55α alone (left), and IER5 alone (right), colored on a sliding scale from blue to red (blue: basic, red: acidic). The catalytic and scaffolding subunits have been removed for clarity in (**c**) and (**d**).

Fig. 3: Intermolecular contacts between B55α and IER5. a, b, Close-up views of the interface between B55α and IER5. IER5 is rendered as a cyan cartoon and side-chains in contact with B55α are rendered as sticks. B55α is rendered as a magenta cartoon under a transparent surface colored by electrostatic surface charge on a sliding scale from blue to red

(blue: basic, red: acidic), with side-chains in contact with IER5 rendered as yellow sticks. The "top" of the interface, which is predominantly hydrophobic, is shown in **(a)**, and the base of the interface, which is dominated by charge-charge interactions, is shown in **(b)**. **c,** Sites of control mutations analyzed in co-immunoprecipitation and functional assays. The labels for IER5 residues are red at the hydrophobic interface **(a),** blue at the charged interface **(b),** and black at the sites of the control mutations in **(c). d,** Western blot analysis of anti-HA immunoprecipitants prepared from I5 cells expressing wild-type or mutant IER5 tagged with FLAG and HA. Labels of the mutants above the blot are color coded according to the labeling scheme for IER5 in **(a-c)**.

Fig. 4: Effects of IER5 mutations on downstream signaling responses. a, Experimental design for controlled activation of Notch1 by GSI washout. The readout for IER5 dependent is the induction of *KRT1* expression (figure design adapted from ref. 9). **b,** RT-qPCR analysis of *KRT1* RNA abundance measured 72 h after GSI washout in I5 cells expressing wild-type or mutant IER5. Transcript abundance was normalized against GAPDH. All data points were obtained in biological sextuplicate. Error bars represent standard deviations of the mean. *, $p<0.05$; **, $p<0.01$, ***, $p<0.001$, ****, $p<0.0001$ (Welch t-test).

Extended Data Fig. 1: Structural model of IER5 predicted by Alphafold2[44] . a, Schematic representation of the domain organization of IER5. The IER-homology region is shown in red. **b,** Cartoon representation of the alphafold2 model of IER5, colored by pIDDT value on a sliding scale from blue (pIDDT < 50) to red (pIDDT >90). **c,** Predicted aligned error plot for the IER5 model, colored on a sliding scale from dark green (0 Å) to white (>30 Å).

Extended Data Fig. 2: Biochemical characterization of PP2A and PP2A-IER5 complexes.

a, Schematic illustration of the protein constructs used to prepare PP2A and PP2A-IER5 complexes. Baculoviruses expressing full-length A, B and C subunits of PP2A were used to produce both PP2A and PP2A-IER5 complexes, and a virus expressing the N-terminal 50 amino acids of IER5 was added for production of the PP2A-IER5 complex. **b,** Size exclusion chromatogram of the purified PP2A on a Superdex 200 column. An SDS-PAGE gel of the purified complex is shown to the right of the chromatogram. The small peak at approximately 20 mL elution volume corresponds to the FLAG peptide. **c,** Size exclusion chromatogram of the purified PP2A-IER5 complex on a Superdex 200 column. An SDS-PAGE gel of the purified complex is shown to the right of the chromatogram. Both peaks are PP2A-IER5 complexes; peak 2 was used in all biochemical and structural studies.

Extended Data Fig. 3: Cryo-EM image processing workflow. Cryo-EM processing scheme for PP2a-IER5 reconstruction. Milestone maps are shown to display progression of processing (the discarded, “junk” class is shown as pink, the monomer as orange, the dimer as blue and the combined map as purple). The masks used for local refinement are light blue.

Extended Data Fig. 4: Cryo-EM data quality. a, Representative micrograph of PP2A-IER5 in vitreous ice visualized by cryo-EM on a Titan Krios microscope equipped with a Gatan K3 detector. Scale bar indicates 500 Å. **b,** GS-FSC curves with default CryoSPARC masks. **c,** Orientation distribution of particles (from CryoSPARC) used in preparing the combined map of PP2A-IER5 for model building. **d,** Local resolution map of the combined map generated by CryoSPARC. **e,** Local resolution map of the focused map generated by CryoSPARC. **f,** Cryo-EM focused map for the portion of the model corresponding to IER5.

Extended Data Fig. 5: Comparison of PP2A structures in free and IER5-bound states. Cartoon representation showing superposition of the structure of free PP2A (PDB:3dw8; gray) on the structure of PP2A-IER5 (colored as in **Fig 2a**). Superposition was performed with the B55α subunit. The 22 Å displacement of the C-terminal end of the scaffolding subunit is indicated with a double-headed arrow.

Extended Data Fig. 6: Overlap of the IER5 binding site with residues implicated in binding of different substrates. The binding epitope of IER5 (a) or residues implicated in binding of pTau (b), p107 (c) and PRC1 (d) inferred from mutational studies[10-12] are shown on the B55α surface using blue, magenta, red and yellow, respectively.

Extended Data Fig. 7: Conservation analysis of IER5. Cartoon representation of the alphafold model of IER5[44], colored by conservation according to the Consurf server[45] on a sliding scale from teal (not conserved) to maroon (most conserved).

Table 1 | Cryo-EM data collection, refinement and validation statistics.

PP2A-IER5 (Combined & Focused) EMD-XXX ([https://www.ebi.ac.uk/emdb/EMDXXX) & EMD-XXX ([https://www.ebi.ac.uk/emdb/EMDXXX). PDB XXX ([http://doi.org/]) & PDB XXX ([http://doi.org/]).		
Data collection and processing		
Voltage (kV)	300	
Electron exposure ($e^-/Å^{-2}$)	53.7	
Defocus range (μm)	0.8 – 2.0	
Pixel size (Å)	0.825	
Symmetry imposed	C1	
Initial particle images (no.)	3,950,110	
Final particle images (no.)	1,179,182	
FSC threshold	0.143	
Refinement	**Combined map**	**Focused map**
Initial model used	alphafold	alphafold
Map-sharpening B-factor ($Å^2$)	-123.2	-130.2
Map Resolution (Å)	3.09	3.13
Map resolution range (Å) (per atom position)	1.80-4.80	1.86-5.38
CryoEF	0.67	0.71
Model composition		
Non-hydrogen atoms	10715	6475
Protein residues	1340	808
Ligands	MN: 2	
B factors ($Å^2$)		
Protein	189.80	186.82
Ligand	232.67	--
R.M.S.D. deviations		
Bond lengths (Å)	0.004	0.030
Bond angles (°)	0.824	0.680
Validation		
MolProbity score	2.00	2.07
Clashscore	14.06	19.69
Poor rotamers (%)	1.00	0.00
Ramachandran plot		
Favoured (%)	95.11	95.98
Allowed (%)	4.89	4.02
Disallowed (%)	0.00	0.00

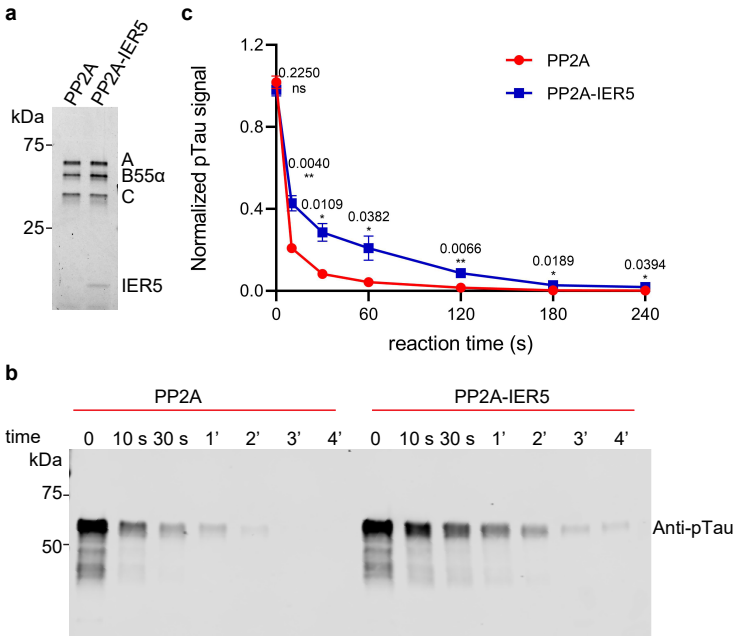
a
PP2A
PP2A-IER5
kDa
75
25
A
B55α
C
IER5
c
Normalized pTau signal
1.2
0.8
0.4
0.0
0.2250
ns
0.0040
**
0.0109
*
0.0382
*
0.0066
**
0.0189
*
0.0394
*
PP2A
PP2A-IER5
0
60
120
180
240
reaction time (s)
b
PP2A
PP2A-IER5
time
0
10 s
30 s
1'
2'
3'
4'
0
10 s
30 s
1'
2'
3'
4'
kDa
75
50
Anti-pTau

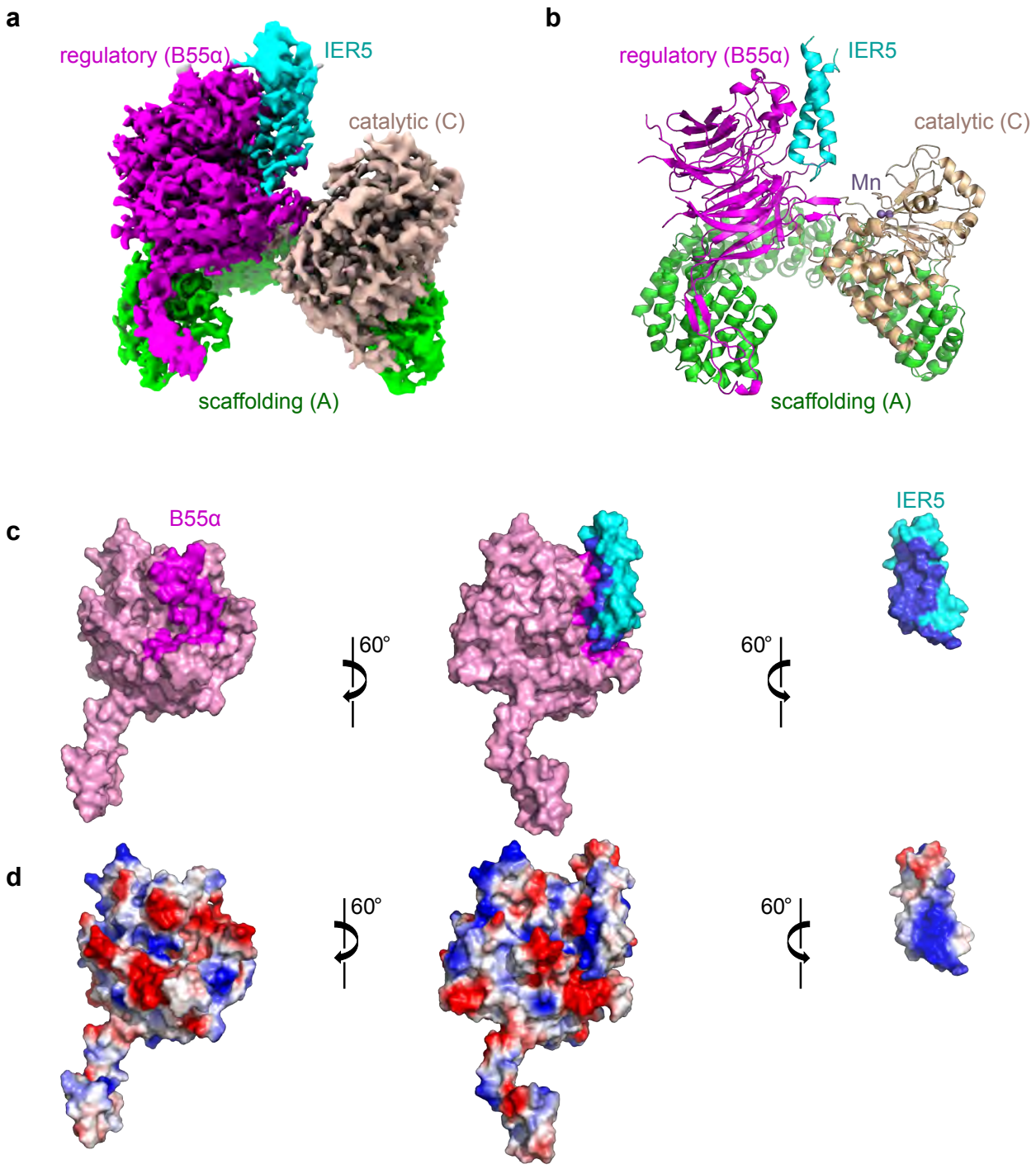
a
regulatory (B55α)
IER5
catalytic (C)
scaffolding (A)
b
regulatory (B55α)
IER5
catalytic (C)
Mn
scaffolding (A)
c
B55α
60°
60°
IER5
d
60°
60°

Fig. 2

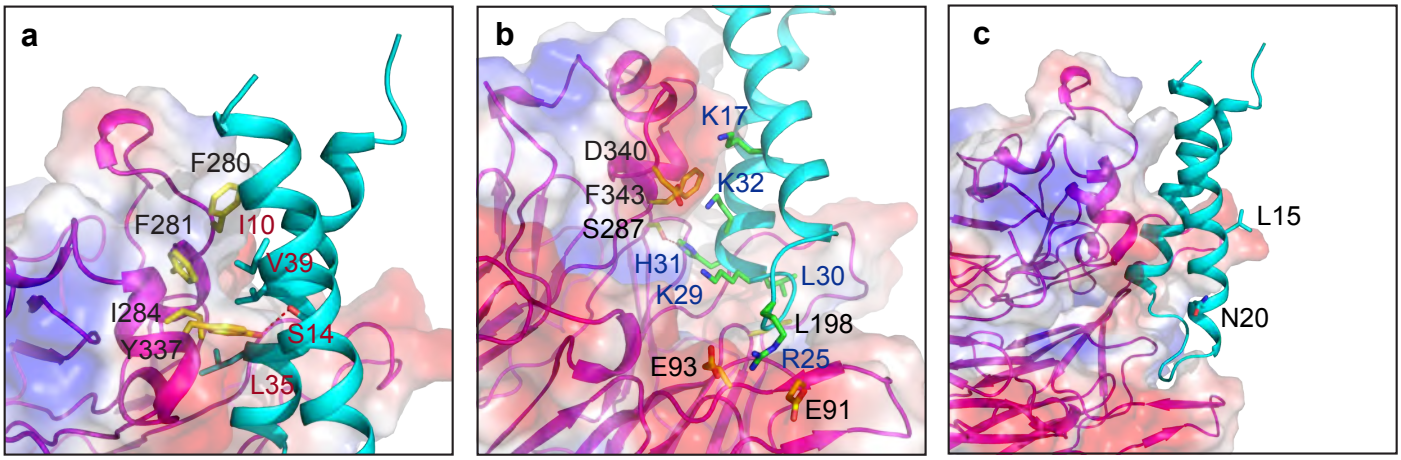
a
F280
F281
I10
V39
I284
Y337
S14
L35
b
K17
D340
K32
F343
S287
H31
L30
K29
L198
E93
R25
E91
c
L15
N20

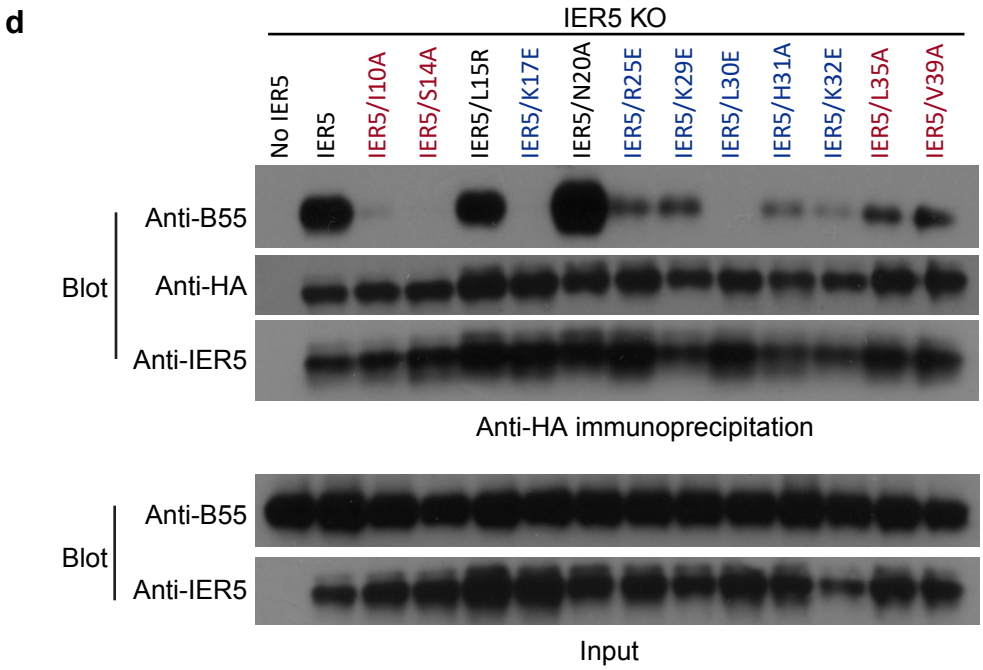
d
IER5 KO
No IER5
IER5
IER5/I10A
IER5/S14A
IER5/L15R
IER5/K17E
IER5/N20A
IER5/R25E
IER5/K29E
IER5/L30E
IER5/H31A
IER5/K32E
IER5/L35A
IER5/V39A
Blot
Anti-B55
Anti-HA
Anti-IER5
Anti-HA immunoprecipitation
Blot
Anti-B55
Anti-IER5
Input

Fig. 3

a

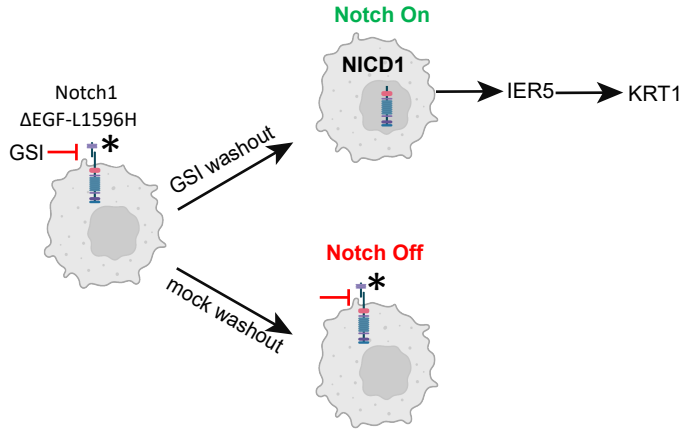
Notch On
NICD1
IER5
KRT1
Notch1
ΔEGF-L1596H
GSI
GSI washout
Notch Off
mock washout

b

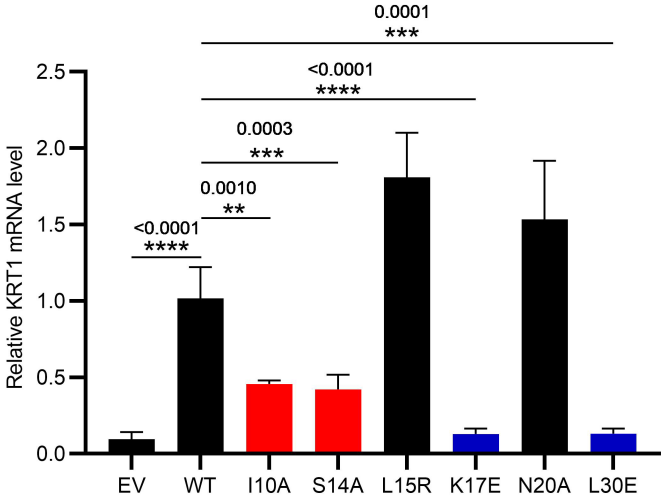
0.0001
***
<0.0001
****
0.0003
***
0.0010
**
<0.0001
****
Relative KRT1 mRNA level
2.5
2.0
1.5
1.0
0.5
0.0
EV
WT
I10A
S14A
L15R
K17E
N20A
L30E

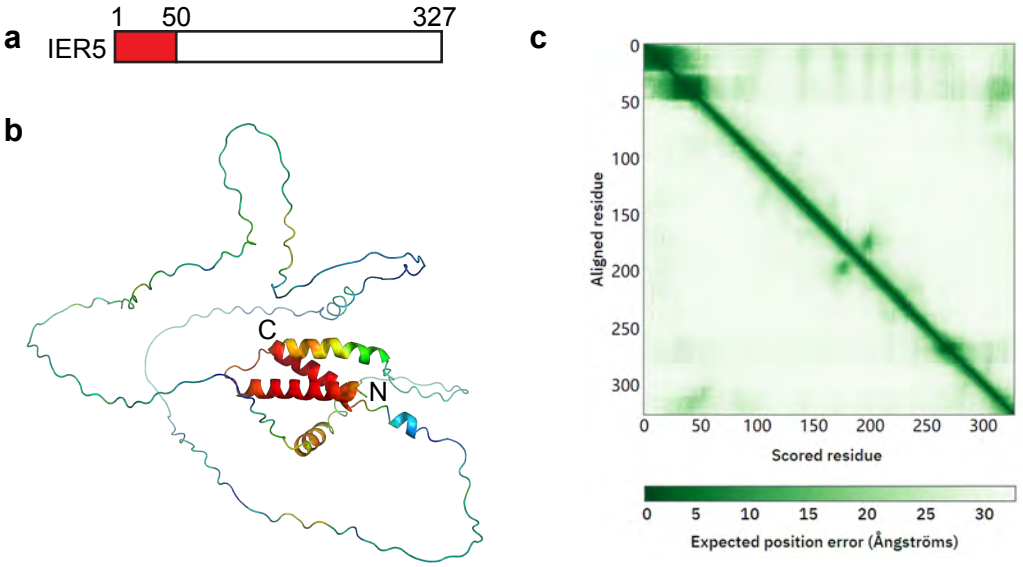

Extended Data Fig. 1

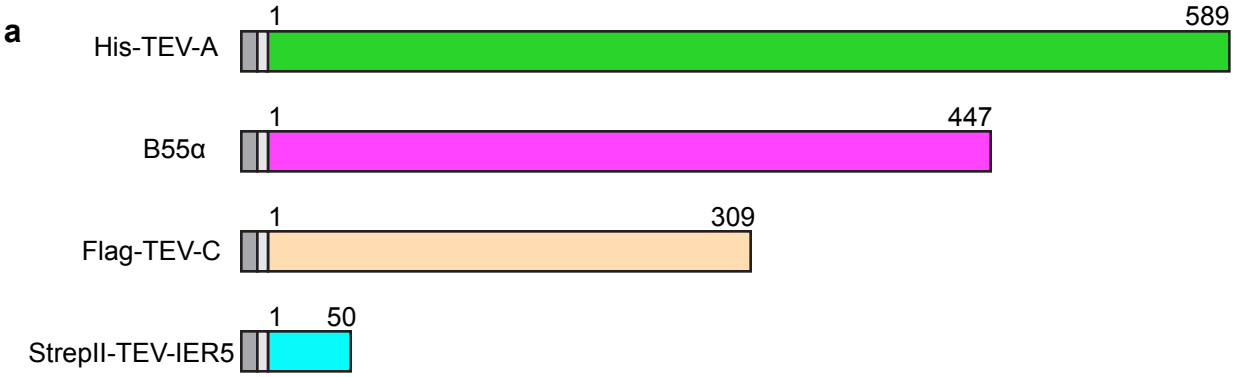

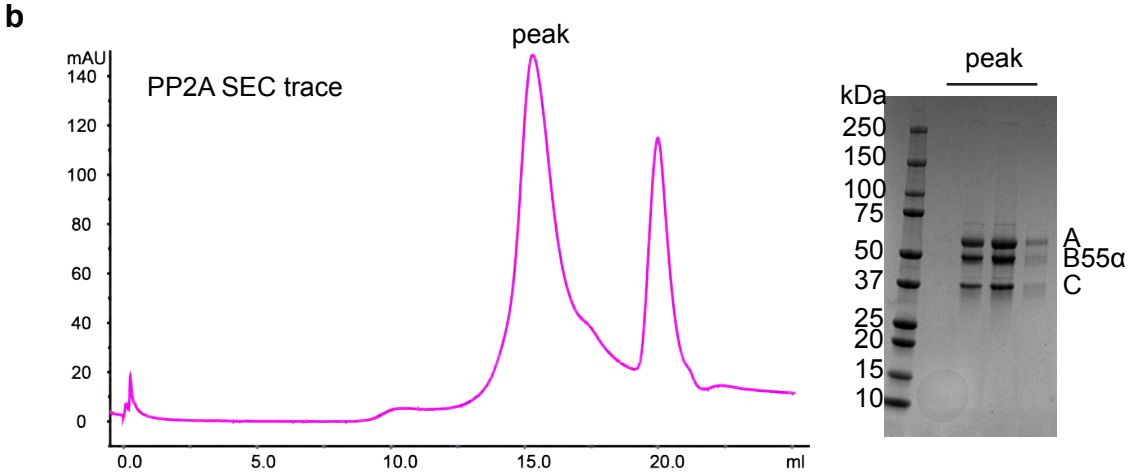

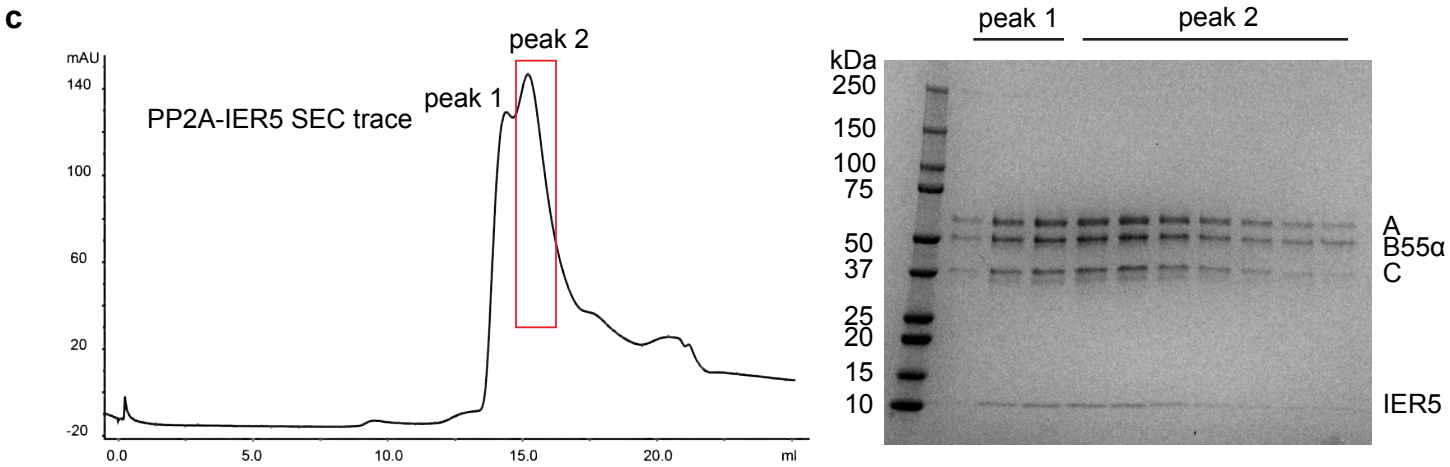

Extended Data Fig. 2

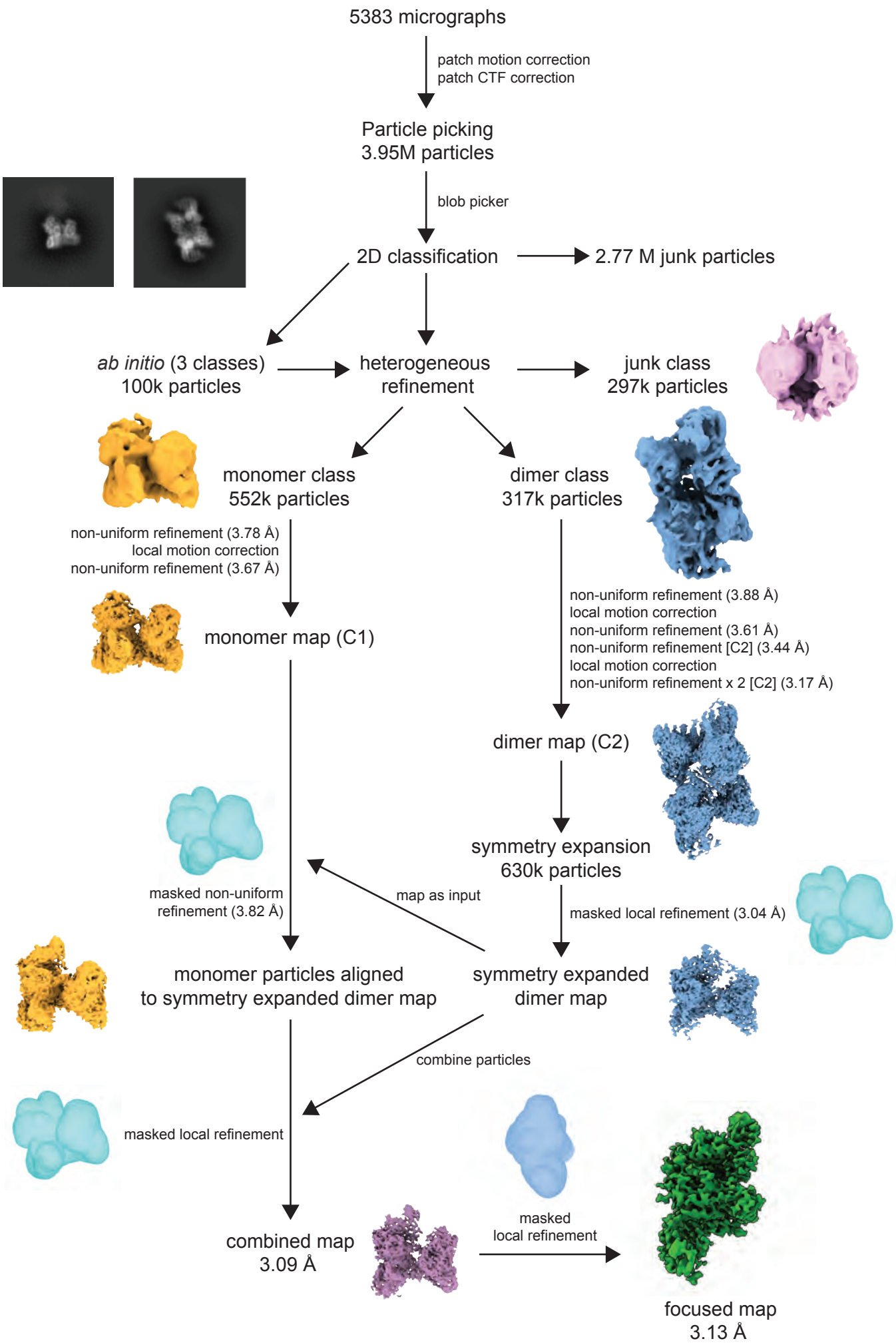

Extended Data Fig. 3

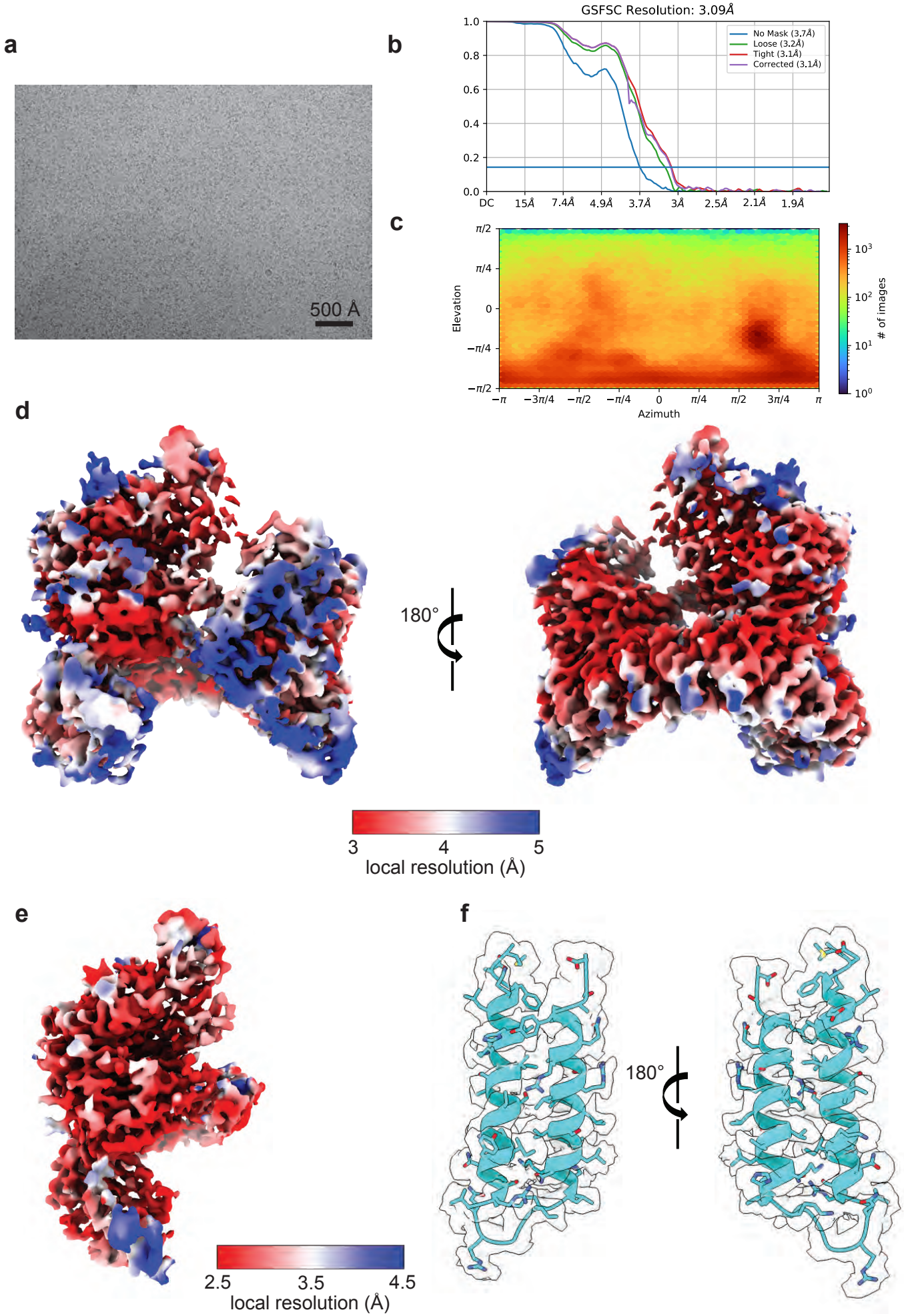

Extended Data Fig. 4

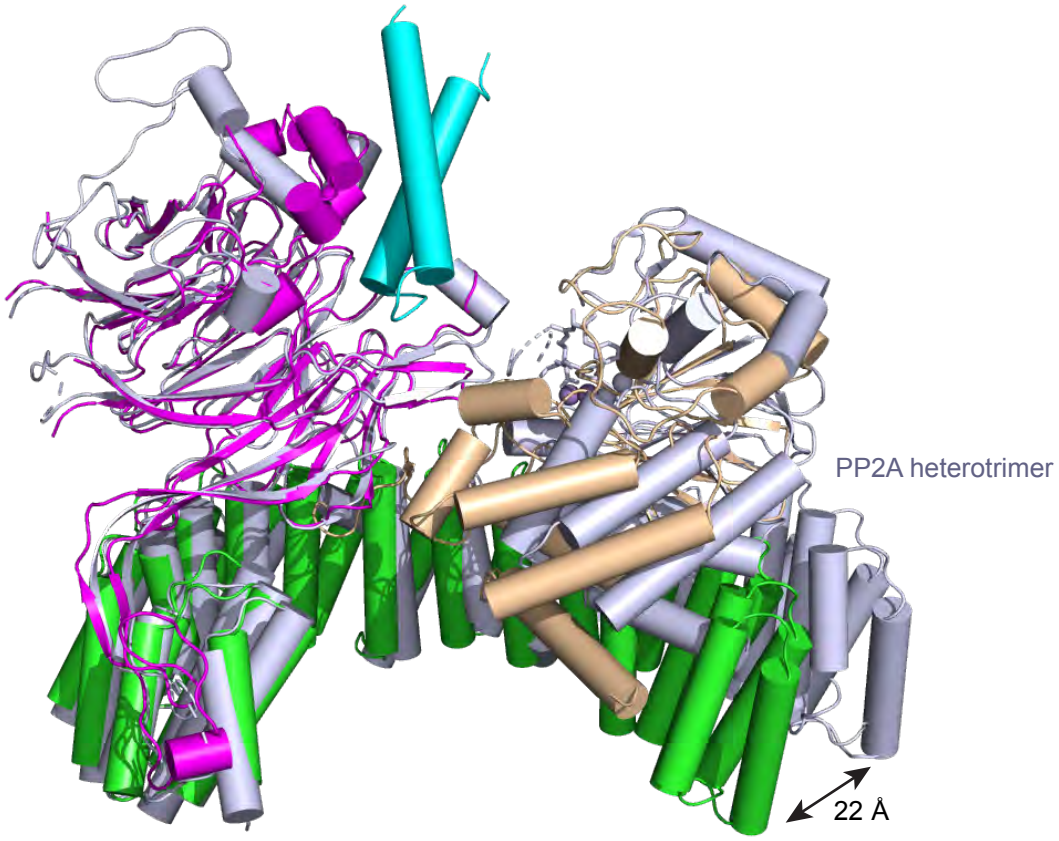

Extended Data Fig. 5

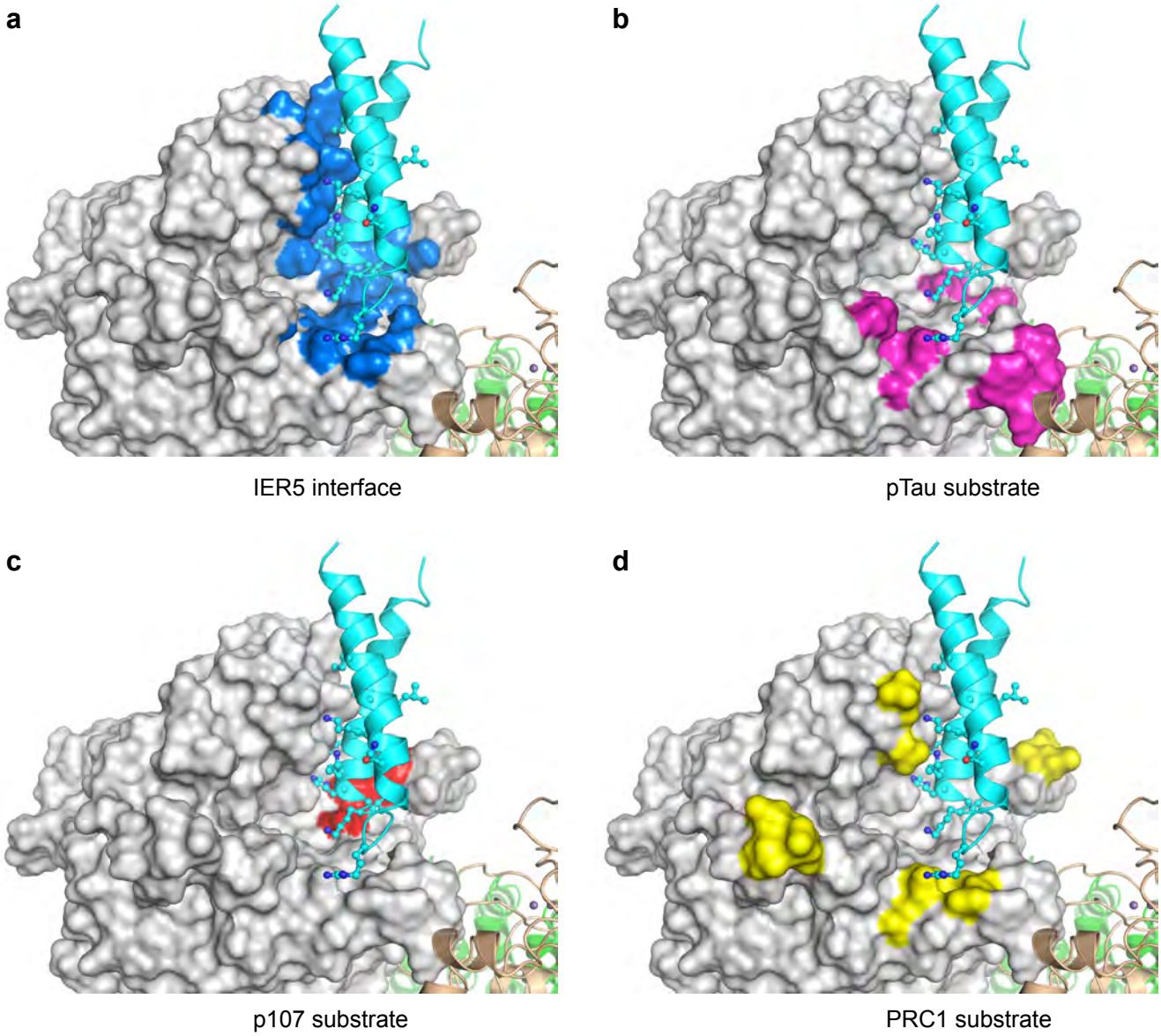

Extended Data Fig. 6

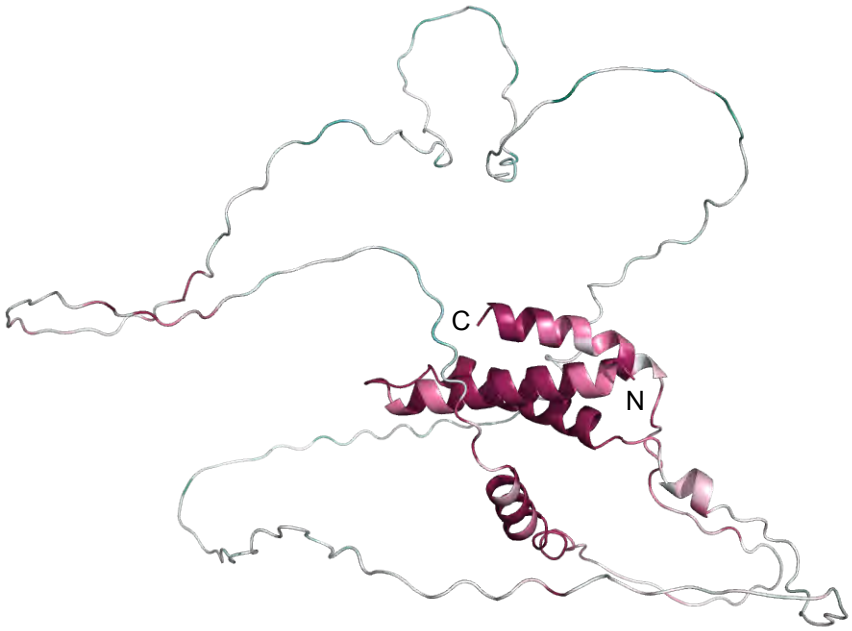

```
1          11         21         31         41
MEFKLEAHRI VSISLGKIYN SRVQRGGIKL HKNLLVSLVL RSARQVYLSD
51         61         71         81         91
PCPGLYLAGP AGTPAPPPQQ QPGEPAAGPP AGWGEPPPPA ARASWPETEP
101        111        121        131        141
QPERSSVSDA PRVGDEVPVA TVTGVGDVFQ GGEADATEAA WSRVEGPRQA
151        161        171        181        191
AAREAEGTAG GWGVTPEVSR AARRPCGCPL GGEDPPGTPA ATPRAACCCA
201        211        221        231        241
PQPAEDEPPA PPAVCPRKRC AAGVGGGPAG CPAPGSTPLK KPRRNLEQPP
251        261        271        281        291
SGGEDDDAEE METGNVANLI SIFGSSFSGL LRKSPGGGRE EEEGEESGPE
301        311        321
AAEPGQICCD KPVLRDMNPW STAIVAF
```

Extended Data Fig. 7